Dynamic Reservoir-Condition Microtomography of Reactive Transport in Complex Carbonates: Effect of Initial Pore Structure and Initial Brine pH

*Menke, H.P.[1]; Bijeljic, B.[1]; Blunt, M.J[1].

[1]Qatar Carbonates and Carbon Storage Research Centre (QCCSRC), Department of Earth Science and Engineering, Imperial College London, SW7 2AZ, London, United Kingdom
*Corresponding Author. email: h.menke12@imperial.ac.uk, phone:+44 07543547195

ABSTRACT

We study the impact of brine acidity and initial pore structure on the dynamics of fluid/solid reaction at high Péclet numbers and low Damköhler numbers. A laboratory μ-CT scanner was used to image the dissolution of Ketton, Estaillades, and Portland limestones in the presence of CO_2-acidified brine at reservoir conditions (10 MPa and 50^{o}C) at two injected acid strengths for a period of 4 hours. Each sample was scanned between 6 and 10 times at ~4 μm resolution and multiple effluent samples were extracted. The images were used as inputs into flow simulations, and analysed for dynamic changes in porosity, permeability, and reaction rate. Additionally, the effluent samples were used to verify the image-measured porosity changes.

We find that initial brine acidity and pore structure determine the type of dissolution. Dissolution is either uniform where the porosity increases evenly both spatially and temporally, or occurs as channelling where the porosity increase is concentrated in preferential flow paths. Ketton, which has a relatively homogeneous pore structure, dissolved uniformly at pH = 3.6 but showed more channelized flow at pH = 3.1. In Estaillades and Portland, increasingly complex carbonates, channelized flow was observed at both acidities with the channel forming faster at lower pH. It was found that the effluent pH, which is higher than that injected, is a reasonably good indicator of effective reaction rate during uniform dissolution, but a poor indicator during channelling. The overall effective reaction rate was up to 18 times lower than the batch reaction rate measured on a flat surface at the effluent pH, with the lowest reaction rates in

the samples with the most channelized flow, confirming that transport limitations are the dominant mechanism in determining reaction dynamics at the fluid/solid boundary.

1. INTRODUCTION

Carbon Capture and Storage (CCS) has been proposed as the primary solution for reducing anthropogenic carbon dioxide (CO_2) emissions. Accurate predictive modelling is imperative for assessing CO_2 storage security (Herzog et al., 2003; Metz et al., 2005). When supercritical CO_2 mixes with carbonate aquifer brine at great depth it forms carbonic acid that can partially dissolve the host rock and alter the storage capacity and permeability of the formation (Langmuir et al., 1997; Morse and Mackenzie, 1990; Peng et al., 2013). The amount and type of dissolution will determine both storage capacity (Li et al., 2006; Rötting et al., 2015) and how the CO_2 and CO_2-acidified brine moves in the subsurface (Johnson et al., 2002; Molins et al., 2012; Steefel et al., 2013). A complete understanding of the brine-rock system is needed to understand and predict the rate of fluid movement and distribution in the aquifer (Daccord et al., 1993a; Daccord et al., 1993b; Maheshwari et al., 2013).

Carbonate dissolution by CO_2 acidified brine is controlled by many factors including pore space heterogeneity, initial pH, and flow conditions (El-Maghraby et al., 2012; Fredd and Fogler, 1998; Luquot and Gouze, 2009). At reservoir conditions the acidity of the brine is strongly dependent on temperature and pressure (Peng et al., 2013). Additionally, the acid pH changes depending on the amount of calcium dissolved in solution (Leal et al., 2013; Peng et al., 2015).

Imaging of dissolution in limestone rock has been performed at the core ($\sim cm$) scale using Computed Tomography (CT). Ott et al. (2012) investigated dissolution where, for several rock types and flow regimes, it was found that reaction of the dissolved CO_2 with the solid matrix increases physical heterogeneity. Ellis et al. (2011) used core-scale imaging to show that exposure to CO_2 progressively reduced the sealing capacity of fractured claystone caprocks. Smith et al. (2012) imaged dissolution of a small dolomitic core before and after reaction with CO_2 acidified brine. Lamy-Chappuis et al. (2014) used CT

scanning to measure calcite dissolution in calcareous gritstone and found that the permeability increase with porosity did not agree with classical models and that the dissolution rate was largely due to the acid supply. Tutolo et al. (2014) examined dolomite dissolution in the presence of CO_2 saturated brine and found evidence of dissolution at low temperatures followed by exsolution and precipitation as the temperature increased. Ott and Oedai (2015) examined carbonate dissolution in the presence of two-phase flow and found large differences in dissolution regimes depending on the CO_2 saturation.

Core–scale imaging is valuable because it is three-dimensional and can be temporally resolved. However, it has a maximum resolution of ~50 μm and thus can only detect the fluid/solid boundary of large features such as fractures and wormholes. The greater portion of the pore space is only resolved as an average greyscale value that blurs or eliminates the solid/liquid interface thus making segmentation and analysis of local changes in connectivity and reaction rate difficult. There are relatively few experiments that investigate the impact of coupled dissolution and flow phenomena at the micron scale – observations that are necessary for the digitisation of the pore network for direct numerical simulations of both flow and transport.

X-ray microtomography (μ-CT) is an accepted method of studying pore-scale processes (Blunt et al., 2013; Gouze and Luquot, 2011). μ-CT creates three-dimensional images with a high spatial resolution (~1 μm) non-invasively. Two types of light sources are used for μ-CT imaging: synchrotron and laboratory. Synchrotron light sources are only sporadically accessible, but have powerful x-ray beams that can take images very quickly. Laboratory scanners are less expensive and more widely available, but have a weaker x-ray source that must be carefully fine-tuned to study dynamic processes. Carbonate rocks are extremely diverse and complex (Archie, 1952) and thus it requires many experiments to determine the principal controls on dissolution for a range of carbonate rock types. Therefore, the development of a laboratory-based technique that allows for reservoir condition imaging of complex pore-structures with a temporal resolution sufficient to study dynamic processes is imperative for acquiring the breadth of data needed for complete understanding of pore-scale processes in carbonate rocks. In an imaging experiment, the reaction rate

102 can be calculated from the measured change in porosity. However, it is not
103 possible to assess the accuracy of this approach without effluent analysis. Thus
104 it is also important to complement image-based measurements with more
105 conventional geochemical sampling. In this paper we present a benchmark
106 comparison between imaging and geochemical sampling using a new laboratory
107 method described below.
108 There have been several studies that have successfully used μ-CT to study
109 dynamic pore-scale processes. Berg et al. (2013) and Andrew et al. (2015) both
110 used a synchrotron light source to look at dynamic pore-scale displacement
111 events between multiple fluid phases with around ~1 min temporal resolution.
112 Other work has looked at fluid/solid reaction in complex carbonates, but were
113 either not performed at reservoir conditions, or were limited to the study of pre
114 and post reaction images (Hao et al., 2013; Luquot et al., 2014; Noiriel et al.,
115 2013; Smith et al., 2013). Menke et al. (2015) imaged the dissolution dynamics of
116 a limestone with a relatively simple pore structure at reservoir conditions and
117 found that the dissolution was uniform throughout the sample along the axis of
118 flow. Menke et al. (2016) examined the dissolution of two heterogeneous
119 carbonates at two flow rates and found a new dissolution regime, channelling, in
120 which conditions for formation were dependent on initial pore topology rather
121 than flow conditions. However, all used an initial brine pH of 3.1 and neither set
122 of experiments included effluent analysis, while the samples were either limited
123 to homogenous rocks that were relatively easy to image, or were performed
124 using a synchrotron light source with specialized equipment.
125 This paper describes reactive dissolution processes at reservoir
126 conditions at the pore scale in both homogenous and heterogeneous carbonates
127 using a laboratory scanner and investigates the impact of initial brine pH on
128 dissolution regimes combined with effluent analysis. We will focus on measuring
129 pore-scale effective reaction rates between two CO_2-acidifed brines of pH = 3.1
130 and 3.6 and limestone rock. We observe two distinct dissolution regimes –
131 uniform and channelling – whose emergence and rate of development are
132 dependent on initial structural heterogeneity and initial brine pH.
133 To investigate the effect of pore-scale heterogeneity we have selected
134 three limestones: Ketton, Estaillades and Portland. Ketton has been shown to

have homogeneous flow characteristics, in that the distribution of velocities computed on an image before reaction is narrower than observed for Estaillades and Portland (Bijeljic et al., 2013a; Bijeljic et al., 2013b). We present a dynamic *in situ* study of carbonate dissolution at reservoir conditions with effluent sampling to track the calcium concentration. Image sequences are binarized and then analysed for porosity and surface area changes. Furthermore, the images are used as input into flow models to elucidate the evolution of permeability and pore-scale velocity fields. Additionally, effective reaction rates are calculated for both effluent samples and CT images and compared, demonstrating both the accuracy of μ-CT imaging of fluid-rock reaction and the formation process of different dissolution structures.

2. METHODS

2.1 Sample selection

To investigate the effect of pore-scale heterogeneity three limestone carbonates are examined: Ketton, Estaillades, and Portland Basebed. These samples were chosen because they were readily available, relatively chemically pure, and diverse in pore structure. Core plugs used for bulk scale analysis were drilled from the same 1 m^3-block of rock as experimental samples to minimize local heterogeneity. The pore throat radii calculated from the Mercury Intrusion Capillary Pressure (MICP) curves are show in Figure 1 and the bulk rock characteristics are listed in Table 1. Portland has a unimodal porosity while both Ketton and Estaillades have bimodal pore structures. However, only the larger porosity modes in Ketton and Estaillades are accessible to μ-CT scanning at 4-µm resolution. All pores below the resolution of 4-µm are classified as microporosity in this study.

2.2 Experimental apparatus

The Zeiss Versa XRM-500 μ-CT scanner was used to image reaction between calcite and CO_2 saturated brine at reservoir conditions. Using our *in situ*

apparatus [Figure 2], ~1 cm long 4 mm diameter carbonate cores of Ketton, Estaillades, and Portland Basebed limestone were reacted by injecting both pH 3.6 and pH 3.1 supercritical (sc) CO_2 saturated brine.

Supercritical CO_2 and 1% *wt* KCl 5% *wt* NaCl brine were pre-equilibrated at experimental conditions (10 MPa & 50^{o}C) in a heated Hastelloy reactor with an entrainment stirrer. Powdered particles of the host rock were used to raise the pH to 3.6 for three of the experiments. An effluent sample was taken from the reactor at the beginning of each experiment to verify initial pH (V5 & V3 in Figure 2); however, as we show later, once reaction was established the pH in the rock, as determined from the effluent, was around 1 unit higher than the injected value.

Once fully saturated, the brine was pulled through the core at a constant flow rate of 0.1 mL.min^{-1}. Tomographic images were taken successively for 4 hours at the centre of the core with a 4 mm field of view. Only the centre of the core was imaged in order to take as many dynamic images as possible during the experimental time.

A thermocouple inserted into the radial port of the Hassler cell coupled with Kapton® heating tape and a proportional integral derivative controller regulated cell temperature to within 1^{o}C. The high-pressure ISCO (www.isco.com) syringe pumps regulated flow accurately to 0.001 mL.min^{-1}. The core was wet initially with a highly-absorbing 25% *wt* KI unreactive brine that made arrival of the low absorbing reactive brine from the reactor easy to observe and made dead volume calculations unnecessary.

Sample heterogeneity determines the speed at which accurate scans can be taken, as more complex and smaller structures require larger numbers of projections to image with sufficient edge sharpness for segmentation. Each rock was first scanned without any fluid at 2400 projections to create an extremely sharp map of the pore space before reaction. Then reactive flow was started and between 6 and 10 scans were taken successively as fast as the scanner allowed with between 400 and 800 projections to resolve the large changes in structure over the course of 4 hours.

2.3 Effluent extraction and calculation of pH

Effluent extraction was carried out during the entire 240 minutes imaging period. 2 mL of effluent was extracted from the effluent stream using a VICI (www.vici.com) electronically actuated 2-position 6-port high pressure high temperature HPLC valve (Figure 2, V12) outside the μ-CT structure approximately every 40 minutes. As the sampling loop contained 2 mL of fluid and the flow rate in the experiments was 0.1 $mL.min^{-1}$, each sample represents the average fluid over a 20-minute period. Samples were immediately acidified using a 2% *wt.* HNO_3 solution and then analysed for [Ca^{2+}] using an ICP-MS. The pH was then computed using the geochemical equations found in Leal et al. (2013) using the Ca^{2+} concentration in the effluent as input and assuming that the brine remains fully saturated with CO_2.

2.4 Image processing

The raw projections were reconstructed and artefacts and beam hardening removed with the Zeiss (www.zeiss.com) proprietary imaging software. The 2000^3 images were binned on the camera to increase signal to noise resulting in a 1000^3 image of ~4 μm voxel size. Further processing was performed by the image processing modules in Avizo 9.1 program (www.vsg.com).

The images [Figure 3] were first filtered using the non-local means filter (Buades et al., 2005; Buades et al., 2008). The first scan in the series is the dry, unreacted scan of the core, has 2400 projections and constitutes time = 0 min. This high projection rate means that the image is very sharp, small pores are very clearly resolved and thus can easily be segmented. High projection rates are only possible for experiments where scan times are long and thus it is not possible to do *in situ* imaging at such high rates. However, taking a high-quality scan before starting the experiment has the advantage of preserving this spatial information for later integration.

All images were registered to the first scan in each series (hereafter called the reference scan) with normalized mutual information. The scans were then resampled to the reference scan grid using the robust Lanczos method (Lanczos,

1950) so that dynamic changes could be computed on a voxel by voxel basis. The greyscale reference scan was then segmented using the watershed segmentation method (Schlüter et al., 2014) resulting in a binary image of the unreacted core.

Dynamic scans of highly heterogeneous rocks during dissolution are difficult to segment because the rock-fluid boundaries are not sharp both due to the boundaries changing during the scan and the low projection rate which means that the small pores and small surface features are not clearly resolved. Thus, we use the difference image approach to segmentation (Menke et al., 2016). A difference image was computed between the greyscale reference and reacted scans that was then filtered and segmented by watershed created a segmented version of the changing pore space. The segmented difference image was then subtracted from the segmented dry scan to achieve a segmented image for each time step.

The pore space was then separated into areas with and without reaction for analysis of the effect of local flow on reaction rate [Figure 4]. The segmented difference between two consecutive images [Figure 4a,b] was obtained [Figure 4c]. The entire pore space of the first image [Figure 4d] was then individually labelled for each unconnected channel on each slice [Figure 4e]. These labels were then separated into labels that intersect with the reacted voxels in the segmented difference image and labels that do not intersect [Figure 4f]. In this way it is possible to isolate the channels with reaction from channels without reaction.

2.5 Flow Modelling

Flow through the pore space of the segmented images was computed by solving both Navier-Stokes and the volume conservation equations using the finite volume method in OpenFoam as described in Bijeljic et al. (2013b); Raeini et al. (2012). We apply a constant pressure boundary condition at the inlet and the outlet faces of the images, whereas no-slip boundary conditions are implemented on the other faces. Each voxel in the segmented images is a grid block in the flow simulator that computes velocities at the grid block centres. Later in the Results section we visualise the ratios of the magnitude of u at the

voxel centres divided by the average pore velocity $U_{av}=q/\phi$, where q is the Darcy velocity in m.s^{-1} and ϕ is the porosity, to study dynamic changes in the velocity fields both in the full pore space, and only in the channels which later react.

3. RESULTS

We study the impact of reaction rate and initial pore structure on dissolution for three limestones: Ketton, Estaillades, and Portland Basebed [Table 2]. First, in experiments 1 and 2, brines of pH = 3.1 and 3.6 are injected into Ketton limestone to investigate the impact of reaction rate on dissolution. Then in experiments 3-6 the more heterogeneous limestones, Estaillades and Portland, are reacted using the same conditions to study the impact of physical heterogeneity.

The images are first binarized and analysed for changes in porosity and surface area. Then a flow solver is run on the segmented images to examine the dynamic changes in permeability and pore velocity. Additionally, we calculate the time-resolved changes in the dimensionless numbers that are traditionally used to describe flow and reactive conditions. Moreover, we examine the predicted overall reaction rate from effluent analysis versus the reaction rate observed by dynamic x-ray microtomography.

3.1 Porosity, Permeability, and Surface Area

Each segmented image series was analysed for changes in porosity by counting the number of voxels of pore and rock. Figure 5 depicts the slice-averaged porosity along the axis of flow for each image through time. Porosity increases with time during dissolution and in all six experiments the porosity increased relatively uniformly along the axis of flow with the exception of Estaillades, which showed slightly more dissolution near the inlet. In experiment 1 the porosity also increases uniformly through time. Conversely, in experiments 2-6 the majority of the porosity increase occurs in the first 120 minutes. As expected, the porosity increases faster with a lower pH when experiments 3, 4, 5,

and 6 are compared. However, the total increase in porosity is highest for experiment 1 (24%) and lowest for experiment 6 (6%) and thus the total amount of dissolution does not appear to be strongly correlated with the pH of the reactive fluid.

Permeability was calculated directly on the segmented images using Darcy's law: we use the fluid viscosity, the average pressure gradient across the sample, and the average flow speed at the outlet computed using the Navier-Stokes solver.

Figure 6 depicts the evolution of porosity and permeability for Ketton, Estaillades, and Portland carbonates at an injected brine pH of 3.1 and 3.6. The change in porosity with time is relatively steady for Experiment 1 [Figure 6a]. However, there are dramatic decreases in the rate of change at later times for experiments 2-6 with this being more marked for those rocks with the greatest initial pore-space heterogeneity.

Figure 6d depicts the evolution of the specific surface area, S during dissolution. S was calculated by summing the number of void voxel faces adjacent to grains on the segmented images. S [m^{-1}] is the surface area [m^2] divided by the bulk volume [m^3]. S initially increases sharply for all experiments, and then remains relatively steady at later times for experiments 2-6, but continues on an upward trend for experiment 1. We note that the initial specific surface area is almost two times higher for Estaillades, which may partially explain the increased dissolution at the sample inlet as there are more reactive surface sites to encourage dissolution along major flow paths.

3.2 Pore-scale Velocity Fields

The pore-scale velocity fields are visualised for Ketton, Estaillades, and Portland carbonates [Figure 7] by calculating the ratios of the magnitude of u at the voxel centres divided by the average pore velocity, U_{av} [$m.s^{-1}$], which is the Darcy velocity q divided by the scan porosity ϕ_{CT} taken from the segmented image. As the flow rate is held constant by the pumps throughout the experiment, the Darcy velocity is also constant. In experiment 1, there are several flow paths through the rock that widen through time. Conversely in

experiments 2, 3, 4 there are many flow paths that consolidate to a single preferential pathway. In experiments 5 & 6, there are initially a small number of pathways that widen at later times.

Figure 8 depicts the probability density functions (PDFs) of velocity. The velocity histogram is computed on the pore-space images and sampled uniformly in 256 bins of $\log(|\boldsymbol{u}|/U_{av})$, which are calculated as the ratios of the magnitude of u at the voxel centres divided by the average pore velocity U_{av}. Ketton has the narrowest distribution, but this still spans approximately 5 orders of magnitude. With increasing heterogeneity, we see a wider distribution for Estaillades, while for Portland we see voxel velocities over 10 orders of magnitude. For experiment 1, in Ketton, there is very little change in the velocity distribution, which indicates that the dissolution is relatively uniform. However, by the end of experiment 2 there is evidence of a sharp peak at high velocity and a rounded peak at lower velocities that suggests a preferential flow path and regions of slower flow. In experiments 3-6 [Figure 8c-f], the PDFs initially show two distinct regions of stagnant and high velocity flow. However, as dissolution progresses the greater proportion of velocities gradually shift to the high velocity region and the stagnant region diminishes. At lower pH this shift toward higher velocity happens more quickly.

3.3 Dimensionless numbers and Reaction Rates

We define the Péclet number *Pe*, Damköhler number *Da*. *Pe* [-] is the pore-scale ratio of diffusive to advective times:

$$Pe = \frac{U_{av}L}{D} \tag{3}$$

where D is the molecular diffusion coefficient of Ca^{2+} at 25°C (7.5×10^{-10} $m^2.s^{-1}$), U_{av} [$m.s^{-1}$] is the average pore velocity, and L [m] is the characteristic length. $L = \pi/S$ where S [m^{-1}] is the specific surface area (Mostaghimi et al., 2012).

We use the flow rate of 0.1 $mL.min^{-1}$ and the specific surface area measured from the segmented images to calculate a characteristic length L of

between 251 μm and 458 μm and a *Pe* of between 394 and 822 for the six experiments [Table 3]. *L* and *Pe* are lowest for Estaillades which has a high specific surface area and highest for Portland which has the lowest porosity (and thus the highest U_{av}). At these high Péclet numbers fresh reactant is readily available throughout the core since the spatially averaged advection is much faster than diffusion.

The Damköhler number [-] is defined as the ratio of advective to reactive times:

$$Da = \frac{\pi r}{U_{av} n} \quad (4)$$

where r is the reaction rate constant of pure calcite, n is calculated using $n = \rho_{calcite}[1-\phi_{total}]/M_{calcite}$, $\rho_{calcite}$ is the density of pure calcite (2.71×10^3 kg.m^{-3}), and $M_{calcite}$ is the molecular mass of calcite (0.1 kg.mol^{-1}). ϕ_{total} , the total porosity, is measured using helium pycnometry for Ketton (ϕ_{total} =0.2337) and Estaillades (ϕ_{total} = 0.295) (Andrew et al., 2014) and measured using nitrogen pycnometry for Portland (ϕ_{total} = 0.213). Here we describe both the porosity detectable at the resolution of the images, ϕ_{CT}, and micro-porosity. We assume that the intra-granular micro-porosity is unaffected by reaction, which is consistent with less than 0.5% observable difference in raw grey-scale within the grains. Thus we define $\phi_{total} = \phi_{grain}(1 - \phi_{CT}) + \phi_{CT}$ to calculate ϕ_{grain} at the beginning of the experiment: we assume that the value of ϕ_{grain} remains constant throughout the experiment and recalculate ϕ_{total} as ϕ_{CT} increases during dissolution.

It has been proposed by Compton et al. (1989) and experimentally confirmed by Peng et al. (2015) that in an entirely surface controlled reaction regime of pH < 4, calcite dissolution kinetics can be modelled as a first order heterogeneous reaction with the equation:

$$r_{exp} = k\alpha_{H^+} \quad (5)$$

where r_{exp} is the batch reaction rate, k is the reaction rate constant and α_{H+} is the activity of H^+ which is equal to 10^{-pH}. In this model the system is assumed to be at

equilibrium at the surface and thus the reaction quotient is 1. Using the r_{exp} at our experimental conditions (10 MPa and 50°C) measured by Peng et al. (2015) at our experimental conditions and a pH 3.1 of 8.1 x 10^{-4} mol.m^{-2}.s^{-1} we can calculate r_{exp} at pH 3.6 to be 2.56 x 10^{-4} mol.m^{-2}.s^{-1}: we use these values to estimate *Da* for the experiments in Table 3.

We can then use dynamic imaging to assess the accuracy of this predicted reaction rate by observing the evolution of the porosity throughout the experiment. As both *Da* and *PeDa* << 1, the reaction rate is slow compared to both the advection and diffusion rates. We then use the change in overall porosity to estimate the average effective reaction rate [mol.m^{-2}.s^{-1}] for each image time-step:

$$r_{eff} = \frac{\rho_{grain}(1-\phi_{grain})}{M_{calcite}S}\frac{\Delta\phi_{CT}}{\Delta t} \quad (6)$$

where $\Delta\phi_{CT}$ is the image-measured change in porosity within the time between the start of each scan, Δt. S [m^{-1}] is the specific surface area at the beginning of that time.

Figure 9 depicts the evolution of *Pe*, *Da*, *PeDa*, and r_{eff} for each experiment. *Pe* [Figure 9a] decreases with time for each experiment with the largest *Pe* decrease in the samples with the most dissolution and the fastest decline of *Pe* in the samples with the most heterogeneity. Conversely *Da* [Figure 9b] has a general increase with all experiments with the greatest increase in experiment 4 and the smallest in experiments 3 & 5. Thus, *PeDa* [Figure 9c] has a small dip at the beginning of reaction for experiments 2-6 but remains relatively constant at later times for all experiments.

The image-measured effective reaction rate declines with time for all experiments, but remains the highest for experiment 1. Experiments 2, 4, & 6 conducted at pH 3.1 have slightly higher initial reaction rates than the experiments conducted at pH 3.6. With the exception of experiment 1 where the reaction rate remains high, the reaction rates decline sharply at later times.

Local Péclet statistics are calculated on each voxel from the velocity distributions of the direct simulations. Each void voxels velocity is normalized to

429 the experimental Darcy velocity and then used with equation 3 to calculate a
430 local Péclet number. Figure 10a shows the maximum *Pe* in the experiments: it is
431 evident that extremely high values can be reached in the centres of the fast-
432 flowing channels. Therefore, there are regions of the pore space where transport
433 is clearly advection-dominated. However, Figure 10b depicts the fraction of void
434 voxels that have a local Péclet number of <1 and have diffusion-dominated
435 transport. The fraction of voxels with diffusion-dominated transport is greatest
436 in the experiments with more heterogeneous pore structure: indeed, they
437 constitute the majority of the pore space in experiments 2-6. These slower-
438 flowing regions are situated at or close to the solid surface: where dissolution
439 occurs, the fluid is relatively stagnant and there are significant diffusive
440 limitations on transport and reaction.
441
442
443 3.5 Effluent Analysis
444
445 Figure 11 depicts the calcium concentration and pH calculated from
446 effluent samples. The concentration of Ca^{2+} [Figure 11a] is measured using an
447 ICP-MS from effluent samples taken during the experiment. We observe the
448 highest Ca^{2+} concentration initially for experiment 1, which then declines slightly
449 through time. In experiments 2-6, the Ca^{2+} concentration starts high (and is
450 higher with a lower injected pH), declines sharply, and then remains relatively
451 steady as the experiment continues.
452 As expected, the pH follows the same trends as the Ca^{2+} concentration
453 with the highest steady values for experiment 1 and lower values for
454 experiments 2-6. Notably, however, the pH is higher than that of the injected
455 brine. It is highest for Ketton, then Estaillades and then Portland, indicating
456 different amounts of transport and reaction in the experiments: this explains
457 why injection pH is not a good indicator of the behaviour for different rocks. The
458 effluent pH is consistent with the ordering of effective reaction rates, Figure
459 9(d): where the reaction is faster, the pH in the effluent is higher.
460
461 4. DISCUSSION

462

463 4.1 Dynamic Porosity-Permeability Relationships

464

465 We fit the data in Figure 6a to an empirical power-law relationship
466 between permeability and porosity. The best fit to the Ketton experiments 1 and
467 2 were $K = 8.03 \times 10^{-8}\ \phi^{5.45}$ and $K = 4.13 \times 10^{-6}\ \phi^{6.93}$ respectively. For the
468 Estaillades experiments 3 and 4 the best fits were $K = 2.36 \times 10^{-2}\ \phi^{13.4}$ and $K =$
469 $5.01 \times 10^{-5}\ \phi^{9.99}$ respectively. For the Portland experiments 5 and 6 we found K
470 $= 2.17 \times 10^{2}\ \phi^{16.2}$ and $K = 6.32 \times 10^{-9}\phi^{23.8}$, respectively. The exponents are higher
471 than the exponent of 3 used in the Kozeny-Carmen relationship and the
472 exponents reported in Menke et al. (2015), but are similar to those reported in
473 Noiriel et al. (2004) for limestone dissolution and Smith et al. (2013) for
474 dissolution of low permeability carbonates. The porosity-permeability
475 relationship follows a trend of increasing exponents with increasing initial
476 heterogeneity with a marked sensitivity to porosity. The pH of the injected brine
477 is a poor indicator of the permeability change. However, the exponents rise with
478 decreasing initial permeability, which suggests a strong correlation between
479 pore-space heterogeneity and the total permeability change.

480

481 4.2 Dynamic Velocity Correlations

482

483 To test our hypothesis that initially present fast flow paths dissolve more
484 quickly than stagnant regions, we use the correlation coefficient presented in
485 Menke et al. (2016). This is defined as:

486

487 $$C(t) = \frac{\sum_{i=1}^{n} v_i(0) v_i(t)}{n} - \frac{\sum_{i=1}^{n} v_i(0)}{n} \frac{\sum_{i=1}^{n} v_i(t)}{n} \quad (1)$$

488

489 with a normalized function:

490

491 $$\overline{C}(t) = \frac{C(t)}{C(0)} \quad (2)$$

492

where $v_i(t)$ is the velocity in voxel i at time t. The computation is only made on voxels that are void in the reference (initial) image at time $t=0$. $C(0)$ is the variance of the initial velocity.

Figure 12 depicts the normalised correlation for all experiments: in all cases this increases over time, indicating that dissolution preferentially occurs in those regions of the pore space that initially had high flow speeds. If instead we had truly uniform dissolution, with reaction occurring at the same rate everywhere, we would expect the correlation function to decline over time. Experiment 1 has the slowest rise in the correlation function and thus is closest to uniform dissolution. Experiments 2-6 show a large rise in C, which provides a quantitative signature for channel formation in regions of the pores space with the highest velocities initially (Menke et al., 2016). Additionally, the correlations are in good agreement with the experiments performed at the same conditions in Menke et al. (2016). We also observe that injected pH is a poor indicator of the correlation in all cases except perhaps in experiments 1 and 2 where the pH changes the dissolution regime and thus the frequency of channelized flow paths.

4.3 Methods of Measuring Reaction Rates

We can compare the mass of dissolved solid predicted from the effluent sample to the mass of dissolved solid observed by μ-CT. The normalised difference, Figure 13, is found from:

$$\Delta CaCO_{3_{(s)}}{}_{\#_{normalised}} = \frac{CaCO_{3_{effluent_{\#}}} - CaCO_{3_{(s)}}{}_{CT_{\#}}}{CaCO_{3_{effluent_{\#}}}} \quad (7)$$

where the mass of solid calcium carbonate remaining in the sample is predicted by effluent analysis by subtracting the cumulative mass of calcium measured in the effluent samples from the mass of calcium carbonate in the initial CT image (time zero) at each time step:

$$CaCO_{3_{effluent_{\#}}} = CaCO_{3_{(s)}}{}_{CT_{time=0}} - \frac{M_{calcite}}{M_{Ca^{2+}}} \sum_{i=0}^{i=\#} \left([Ca^{2+}]_{effluent} - [Ca^{2+}]_{reactor} \right) F \Delta t_i \quad (8)$$

where t is time [s], F is the flow rate [$m^3.s^{-1}$], $M_{Ca^{2+}}$is the molecular mass of Ca^{2+}, $M_{calcite}$ is the molecular mass of calcite, # is the effluent sample number, and $CaCO_{3_{(s)_{CT}}}$ is the total mass of solid calcium carbonate in the core calculated from the initial CT scan. Here the concentrations are measured in $moles.m^{-3}$.

The total mass of calcium carbonate is calculated at each time from the CT images with:

$$CaCO_{3_{(s)_{CT_t}}} = \left(1 - \phi_{total_t}\right)\rho_{calcite}\pi d^2 h \quad (9)$$

where d is the core radius, h is the total core length and $\rho_{calcite}$ is the density of calcite. The ϕ_{total} in the imaged 4 mm portion of the core is used as a proxy for the entire 10 mm length. We believe this is reasonable as the porosity change is relatively constant along the axis of flow in the imaged portion of the core [Figure 5].

We observe an agreement between the CT observed dissolution and that predicted by effluent analysis to within 6%, Figure 13. Most of the time the difference is positive, indicating that effluent analysis may be missing some of the dissolution. This could be due to small particles that are left behind when the effluent sample is transferred from the sampling syringe into test tubes for ICP-MS analysis or slightly differing amounts of dissolution in the unimaged portions of the core.

Moreover, we can use the pH calculated from the effluent samples in the experiment and equation 5 to compare the image-measured reaction rate to assess whether batch- measured effective reaction rates can be used to predict pore-scale effective reaction rates from the effluent-calculated pH [Table 4]. We use the values of pH calculated from the effluent Ca^{2+} concentration and image-measured r_{eff} values from ~180 minutes, which is when we observe that the rate of reaction has reached a quasi-equilibrium state for all experiments. The surface area used in our r_{eff} calculations is the image-measured surface area. Peng (2015) found that the geometric surface area of a cleaved piece of calcite mineral was accurate to within 0.2% for calculating batch reaction rates. We find that the

557 values of pH calculated from the effluent Ca^{2+} concentration are a reasonably
558 good indicator of image-observed reaction rate to within a factor of two for
559 experiments 1 and 3. However, as reactive flow complexity increases and the
560 dissolution regime changes from uniform to channelling the prediction becomes
561 less accurate. Experiments 2 and 4 are predicted to have an effective reaction
562 rate that is 6 times higher than those observed, and experiment 5 and 6 are
563 predicted to be 18 times higher. Had we used the injected pH the discrepancies
564 would have been even larger, with an over-estimate of likely rate by up to a
565 factor of 100.
566 We believe that the discrepancy between predicted and measured
567 reaction rates is due to flow limitations in removing reaction products from the
568 rock surface. Figure 14 depicts the interplay between flow and transport
569 processes during uniform dissolution and channel formation. During uniform
570 dissolution [Figure 14a] the flow velocity distribution is relatively narrow and
571 the majority of the pore space experiences relatively high velocities. Thus, the
572 reaction products are efficiently moved away from the surface of the grains and
573 are swept away down the advective flow streamlines such that fresh reactive
574 fluid is continually exposed to the entire rock surface. This causes the reaction to
575 be relatively uniform, the observed effective reaction rate to be high, and the
576 calculated effluent pH to be high, as the Ca^{2+} concentration in the effluent is
577 representative of the entire pore fluid. This also implies that for these samples
578 the resolution of μ-CT scanning adequately captures the surface area available
579 for reaction in the surface-reaction-controlled regime. However during
580 channelling [Figure 14b], the velocity distribution spans many orders of
581 magnitude and there are many regions of the pore space that do not experience
582 fast flow: see Figure 10b. The majority of the injected reactive fluid moves
583 through the centre of the fast flow paths without encountering or reacting with
584 the rock grains except on the channel walls. Thus, during uniform dissolution the
585 effluent pH calculated is indicative of the average pore-space reaction, while for
586 channelling the effluent pH calculated is only an indicator of the reaction within
587 the fast flow paths, which is considerably less due to the smaller surface area
588 available for reaction. This is confirmed by the recalculation of the image
589 observed reaction rate using only the surface area of the reactive channels [Table

590 4] which shows much better agreement between the predicted and observed
591 effective reaction rates.
592
593 5. CONCLUSIONS
594
595 We have found that the initial brine pH and initial pore structure have a
596 clear influence on the reaction-induced development of porosity and
597 permeability at the pore scale. We observe uniform dissolution in a homogenous
598 carbonate at an injection pH of 3.6 and channelling at pH = 3.1 and high
599 heterogeneity. Additionally, in heterogeneous samples we see faster channelling
600 with increasing heterogeneity and decreasing pH of the injected brine. We find
601 that effluent pH is a reasonably good indicator of effective reaction rate during
602 uniform dissolution. However, pH is a poor indicator of the effective reaction
603 rate during channelling, but can be used to help identify dissolution regime with
604 a lower effluent pH being more likely to be a caused by channelized flow.
605 Moreover, we observe that the overall reaction rates are up to 18 times lower
606 than batch reaction rates at the effluent pH due to transport and flow limitations
607 at the fluid/solid interface: the majority of the pore space is in a diffusion-limited
608 regime even when the average flow rate indicates advection-dominated
609 conditions.
610 Bench-top x-ray microtomography coupled with a reservoir condition
611 flow apparatus and effluent sampling provides an accessible experimental tool
612 that is adaptable to many applications. Our method integrates experiment and
613 modelling to explore the dynamics of reservoir condition reactive flow at the
614 micron scale.
615
616 ACKNOWLEDGEMENTS
617
618 We gratefully acknowledge funding from the Qatar Carbonates and Carbon
619 Storage Research Centre (QCCSRC), provided jointly by Qatar Petroleum, Shell,
620 and Qatar Science & Technology Park. We also thank Ali Raeini and Joao Pereira
621 Nunes for help with the flow simulations.
622

623 REFERENCES

624

625 Andrew, M., Bijeljic, B., Blunt, M.J., 2014. Pore-scale imaging of trapped
626 supercritical carbon dioxide in sandstones and carbonates. International
627 Journal of Greenhouse Gas Control, 22: 1-14.
628 Andrew, M., Menke, H., Blunt, M.J., Bijeljic, B., 2015. The Imaging of Dynamic
629 Multiphase Fluid Flow Using Synchrotron-Based X-ray Microtomography
630 at Reservoir Conditions. Transport in Porous Media: 1-24.
631 Archie, G.E., 1952. Classification of carbonate reservoir rocks and petrophysical
632 considerations. AAPG Bulletin, 36(2): 278-298.
633 Berg, S. et al., 2013. Real-time 3D imaging of Haines jumps in porous media flow.
634 Proceedings of the National Academy of Sciences of the United States of
635 America, 110(10): 3755-3759.
636 Bijeljic, B., Mostaghimi, P., Blunt, M.J., 2013a. Insights into non‐Fickian solute
637 transport in carbonates. Water Resources Research, 49(5): 2714-2728.
638 Bijeljic, B., Raeini, A., Mostaghimi, P., Blunt, M.J., 2013b. Predictions of non-
639 Fickian solute transport in different classes of porous media using direct
640 simulation on pore-scale images. Physical Review E, 87(1): 013011.
641 Blunt, M.J. et al., 2013. Pore-scale imaging and modelling. Advances in Water
642 Resources, 51: 197-216.
643 Buades, A., Coll, B., Morel, J.-M., 2005. A non-local algorithm for image denoising.
644 Computer Vision and Pattern Recognition, 2005. CVPR 2005. IEEE
645 Computer Society Conference on, 2: 60-65.
646 Buades, A., Coll, B., Morel, J.-M., 2008. Nonlocal image and movie denoising.
647 International Journal of Computer Vision, 76(2): 123-139.
648 Compton, R.G., Pritchard, K.L., Unwin, P.R., 1989. The dissolution of calcite in acid
649 waters: mass transport versus surface control. Freshwater Biology, 22(2):
650 285-288.
651 Daccord, G., Lenormand, R., Lietard, O., 1993a. Chemical Dissolution of a Porous-
652 Medium by a Reactive Fluid .1. Model for the Wormholing Phenomenon.
653 Chemical Engineering Science, 48(1): 169-178.
654 Daccord, G., Lietard, O., Lenormand, R., 1993b. Chemical Dissolution of a Porous-
655 medium by a Reactive Fluid .2. Convection vs Reaction, Behavior Diagram.
656 Chemical Engineering Science, 48(1): 179-186.
657 Dong, H., Blunt, M.J., 2009. Pore-network extraction from micro-computerized-
658 tomography images. Physical review E, 80(3): 036307.
659 El-Maghraby, R., Pentland, C., Iglauer, S., Blunt, M., 2012. A fast method to
660 equilibrate carbon dioxide with brine at high pressure and elevated
661 temperature including solubility measurements. The Journal of
662 Supercritical Fluids, 62: 55-59.
663 Ellis, B. et al., 2011. Deterioration of a fractured carbonate caprock exposed to
664 CO2‐acidified brine flow. Greenhouse Gases: Science and Technology,
665 1(3): 248-260.
666 Fredd, C., Fogler, S., 1998. Influence of Transport and Reaction on Wormhole
667 Formations in Porous Media. AIChE, 44(9).
668 Gouze, P., Luquot, L., 2011. X-ray microtomography characterization of porosity,
669 permeability and reactive surface changes during dissolution. Journal of
670 Contaminant Hydrology, 120-21: 45-55.

671 Hao, Y., Smith, M., Sholokhova, Y., Carroll, S., 2013. CO2-induced dissolution of
672 low permeability carbonates. Part II: Numerical modeling of experiments.
673 Advances in Water Resources, 62: 388-408.
674 Herzog, H., Caldeira, K., Reilly, J., 2003. An issue of permanence: Assessing the
675 effectiveness of temporary carbon storage. Climatic Change, 59(3): 293-
676 310.
677 Johnson, J.W., Nitao, J.J., Steefel, C.I., Knuass, K.G., 2002. Reactive transport
678 modeling of geologic CO2 sequestration in saline aquifers: the influence of
679 intra-aquifer shales and the relative effectiveness of structural, solubility,
680 and mineral trapping during prograde and retrograde sequestration,
681 Lawrence Livermore National Laboratory, Livermore, CA.
682 Lamy‐Chappuis, B., Angus, D., Fisher, Q., Grattoni, C., Yardley, B.W., 2014. Rapid
683 porosity and permeability changes of calcareous sandstone due to CO2‐
684 enriched brine injection. Geophysical Research Letters, 41(2): 399-406.
685 Lanczos, C., 1950. An iteration method for the solution of the eigenvalue problem
686 of linear differential and integral operators. United States Governm. Press
687 Office.
688 Langmuir, D., Hall, P., Drever, J., 1997. Aqueous Environmental Geochemistry.
689 Leal, A.M., Blunt, M.J., LaForce, T.C., 2013. A robust and efficient numerical
690 method for multiphase equilibrium calculations: Application to CO2–
691 brine–rock systems at high temperatures, pressures and salinities.
692 Advances in Water Resources, 62: 409-430.
693 Leal, A.M., Blunt, M.J., LaForce, T.C., 2014. Efficient chemical equilibrium
694 calculations for geochemical speciation and reactive transport modelling.
695 Geochimica et Cosmochimica Acta, 131: 301-322.
696 Li, Z.W., Dong, M.Z., Li, S.L., Huang, S., 2006. CO2 sequestration in depleted oil and
697 gas reservoirs - caprock characterization and storage capacity. Energy
698 Conversion and Management, 47(11-12): 1372-1382.
699 Luquot, L., Gouze, P., 2009. Experimental determination of porosity and
700 permeability changes induced by injection of CO2 into carbonate rocks.
701 Chemical Geology, 265(1-2): 148-159.
702 Luquot, L., Rodriguez, O., Gouze, P., 2014. Experimental Characterization of
703 Porosity Structure and Transport Property Changes in Limestone
704 Undergoing Different Dissolution Regimes. Transport in Porous Media,
705 101(3): 507-532.
706 Maheshwari, P., Ratnakar, R., Kalia, N., Balakotaiah, V., 2013. 3-D simulation and
707 analysis of reactive dissolution and wormhole formation in carbonate
708 rocks. Chemical Engineering Science, 90: 258-274.
709 Menke, H.P., Bijeljic, B., Andrew, M.G., Blunt, M.J., 2015. Dynamic Three-
710 Dimensional Pore-Scale Imaging of Reaction in a Carbonate at Reservoir
711 Conditions. Environmental science & technology, 49(7): 4407-4414.
712 Menke, H.P., Bijeljic, B., Blunt, M.J., 2016. Reservoir Condition Imaging of Reactive
713 Transport in Heterogeneous Carbonates Using Fast Synchrotron
714 Tomography – Effect of Initial Pore structure and Flow Conditions.
715 Chemical Geology, 428(1): 15-26.
716 Metz, B., Davidson, O., De Coninck, H., Loos, M., Meyer, L., 2005. IPCC, 2005: IPCC
717 special report on carbon dioxide capture and storage. Prepared by
718 Working Group III of the Intergovernmental Panel on Climate Change.
719 Cambridge, United Kingdom and New York, NY, USA, 442 pp.

720 Molins, S., Trebotich, D., Steefel, C.I., Shen, C., 2012. An investigation of the effect
721 of pore scale flow on average geochemical reaction rates using direct
722 numerical simulation. Water Resources Research, 48(3).
723 Morse, J.W., Mackenzie, F.T., 1990. Geochemistry of sedimentary carbonates.
724 Mostaghimi, P., Bijeljic, B., Blunt, M.J., 2012. Simulation of flow and dispersion on
725 pore-space images. SPE J, 17(4): 1131-1141.
726 Noiriel, C., Gouze, P., Bernard, D., 2004. Investigation of porosity and
727 permeability effects from microstructure changes during limestone
728 dissolution. Geophysical research letters, 31(24).
729 Noiriel, C., Gouze, P., Made, B., 2013. 3D analysis of geometry and flow changes in
730 a limestone fracture during dissolution. Journal of Hydrology, 486: 211-
731 223.
732 Ott, H. et al., 2012. Core-flood experiment for transport of reactive fluids in rocks.
733 Review of Scientific Instruments, 83(8): 084501.
734 Ott, H., Oedai, S., 2015. Wormhole formation and compact dissolution in single‐
735 and two‐phase CO2‐brine injections. Geophysical Research Letters,
736 42(7): 2270-2276.
737 Peng, C., 2015. Chemical Interactions between Carbon Dioxide Acidified Aqueous
738 Fluids and Carbonate Minerals, Imperial College London, 275 pp.
739 Peng, C., Crawshaw, J.P., Maitland, G.C., Trusler, J.M., 2015. Kinetics of calcite
740 dissolution in CO 2-saturated water at temperatures between (323 and
741 373) K and pressures up to 13.8 MPa. Chemical Geology, 403: 74-85.
742 Peng, C., Crawshaw, J.P., Maitland, G.C., Trusler, J.M., Vega-Maza, D., 2013. The pH
743 of CO 2-saturated water at temperatures between 308K and 423K at
744 pressures up to 15MPa. The Journal of Supercritical Fluids, 82: 129-137.
745 Raeini, A.Q., Blunt, M.J., Bijeljic, B., 2012. Modelling two-phase flow in porous
746 media at the pore scale using the volume-of-fluid method. Journal of
747 Computational Physics, 231(17): 5653-5668.
748 Rötting, T.S., Luquot, L., Carrera, J., Casalinuovo, D.J., 2015. Changes in porosity,
749 permeability, water retention curve and reactive surface area during
750 carbonate rock dissolution. Chemical Geology, 403: 86-98.
751 Schlüter, S., Sheppard, A., Brown, K., Wildenschild, D., 2014. Image processing of
752 multiphase images obtained via X‐ray microtomography: A review.
753 Water Resources Research, 50(4): 3615-3639.
754 Smith, M.M., Sholokhova, Y., Hao, Y., Carroll, S.A., 2012. Evaporite caprock
755 integrity: An experimental study of reactive mineralogy and pore-scale
756 heterogeneity during brine-CO2 exposure. Environmental science &
757 technology, 47(1): 262-268.
758 Smith, M.M., Sholokhova, Y., Hao, Y., Carroll, S.A., 2013. CO2-induced dissolution
759 of low permeability carbonates. Part I: Characterization and experiments.
760 Advances in Water Resources, 62: 370-387.
761 Steefel, C.I., Molins, S., Trebotich, D., 2013. Pore scale processes associated with
762 subsurface CO2 injection and sequestration. Reviews in Mineralogy and
763 Geochemistry, 77(1): 259-303.
764 Tutolo, B.M., Luhmann, A.J., Kong, X.-Z., Saar, M.O., Seyfried Jr, W.E., 2014.
765 Experimental observation of permeability changes in dolomite at CO2
766 sequestration conditions. Environmental science & technology, 48(4):
767 2445-2452.
768

769

770

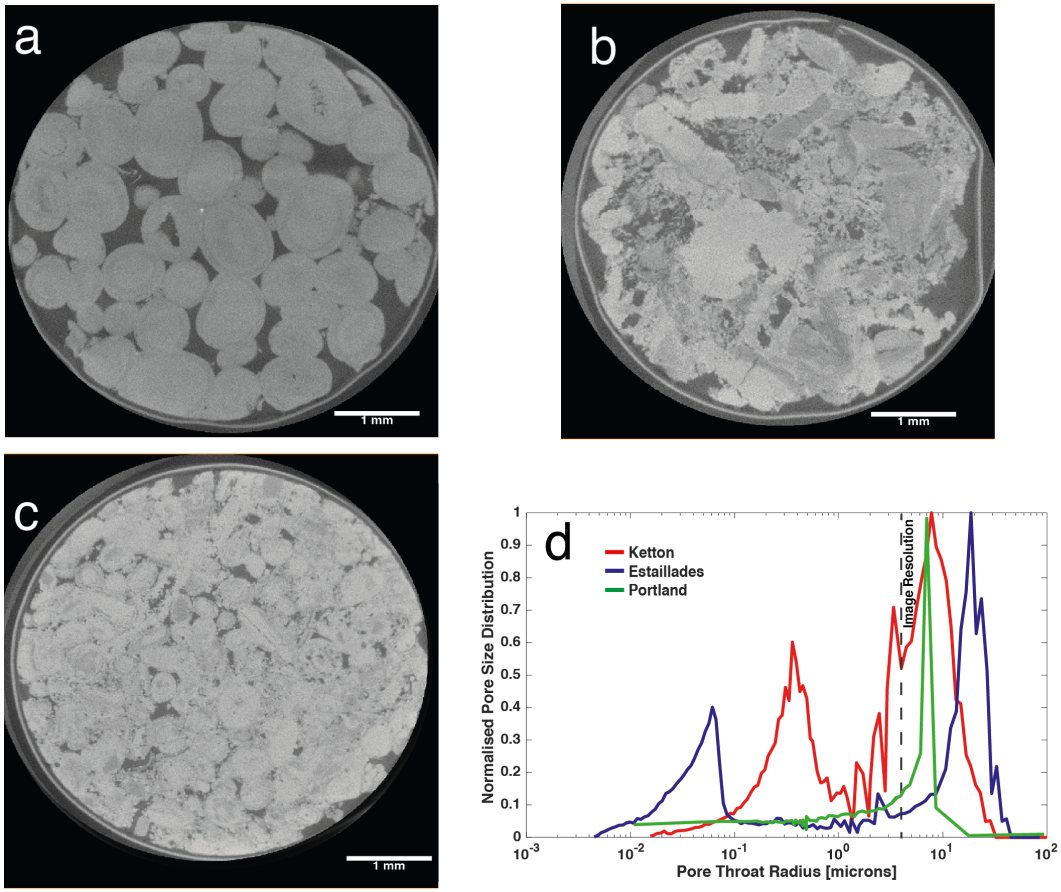

771

772 **Figure 1** 2D μ-CT slices of Ketton (a), Estaillades (b), and Portland Basebed (c)
773 with their normalised pore throat radii distributions (d). The μ-CT image
774 resolution threshold is the black dotted line.

775

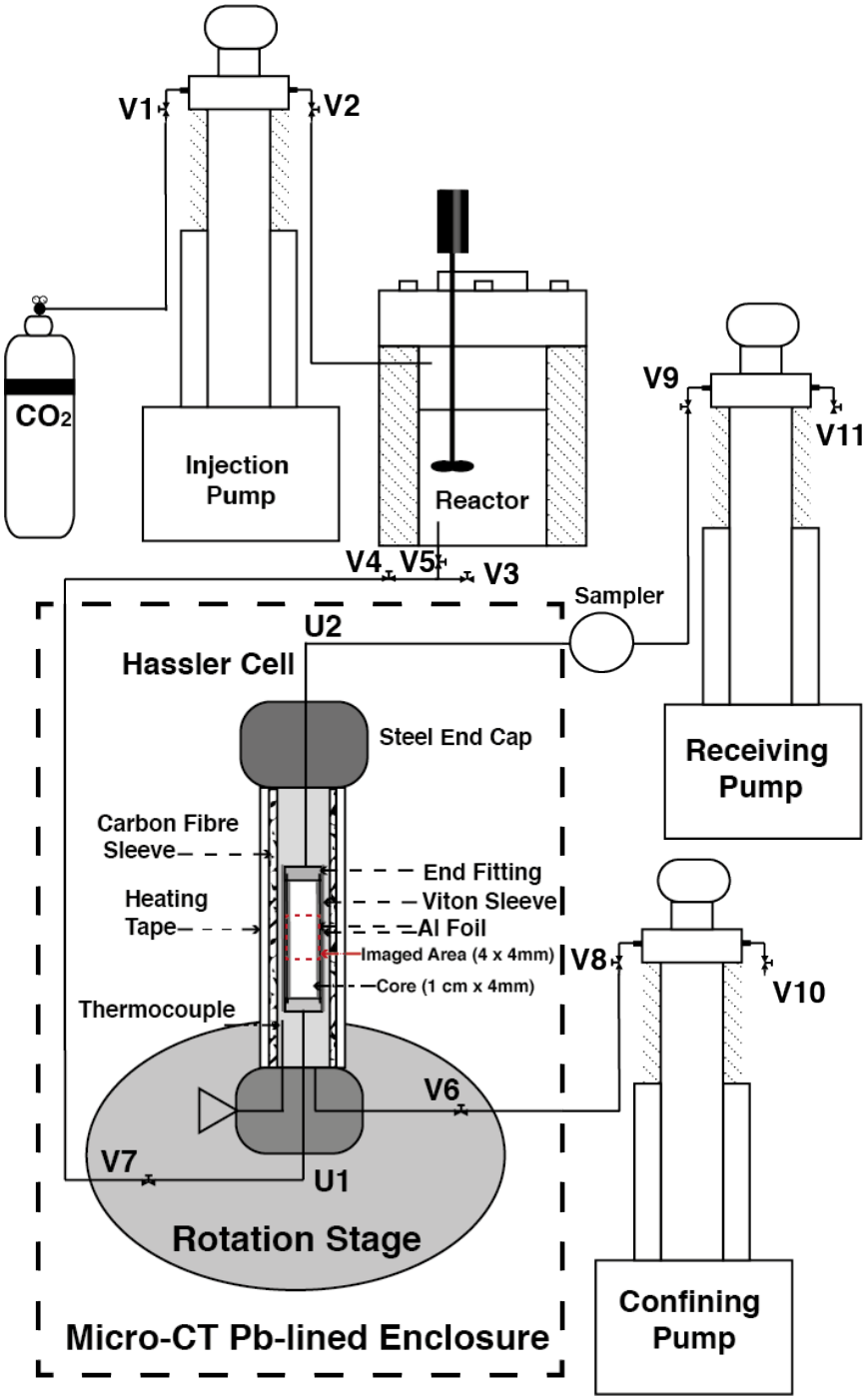

Figure 2 The *in situ* experimental apparatus. CO_2 is pressurized by the injection pump and used to equilibrate brine in the reactor. Reactive brine is pulled through core assembly by the receiving pump. The cell is confined by deionized water in the confining pump and heated using heating tape controlled by a thermocouple in the confining fluid. The experimental system is connected together using tubing and fluid flow is directed using Valves (V) and Unions (U). Effluent from the flow cell is sampled using Valve 12. Modified from Menke et al. (2015).

Table 1 Summary of physical rock properties. Chemical composition was found using X-ray diffraction.

	Ketton	Estaillades	Portland Basebed
Rock type	Limestone	Limestone	Limestone
Origin	Ketton, Rutland, UK	Oppede, France	Portland, UK
Age	169-176 million Years	22 million years	150-190 million years
Bulk-measured total porosity ϕ_T []	0.2337	0.295	0.213
Bulk-measured absolute permeability [m^2]	2.81×10^{-12}	1.490×10^{-12}	5.24×10^{-15}
% Calcite	99.1	97.2	97.9
% Quartz	0.9	2.8	2.1
% Clay	0	0	0
% Feldspar	0	0	0

Table 2 Experimental Parameters

Experiment Number	**1**	**2**	**3**	**4**	**5**	**6**
Rock Name	Ketton Limestone	Ketton Limestone	Estaillades Limestone	Estaillades Limestone	Portland Basebed Limestone	Portland Basebed Limestone
Flow rate [mL/min]	0.1	0.1	0.1	0.1	0.1	0.1
Injected Fluid pH	3.6	3.1	3.6	3.1	3.6	3.1
Temperature [°C]	50	50	50	50	50	50
Pressure [MPa]	10	10	10	10	10	10
Number of Scans	6	10	6	6	6	6
Voxel Size [μm]	4.15	4.07	4.15	4.07	4.15	4.59
Projections	800	400	800	800	800	800
Scan Time [min]	40	20	40	40	40	40
Exposure Time [sec]	1.4	1.4	1.3	1.3	1.4	1.4

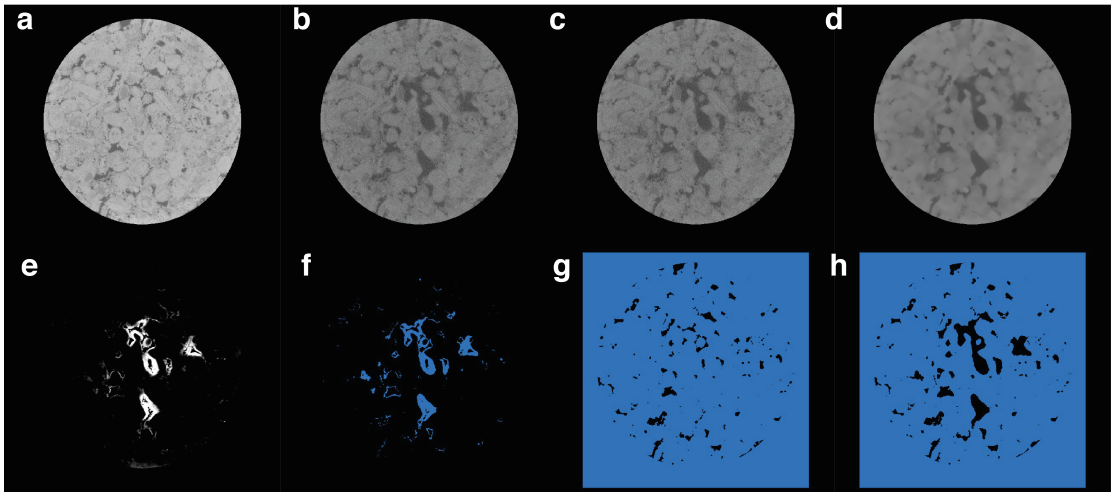

Figure 3 The image analysis workflow. Raw dry scans (a) and wet scans (b) are registered and resampled (c) and then filtered (d). The wet scan is subtracted from the dry scan to create a difference image (e). The difference image is the

segmented (f) along with the dry scan (g). (f) is then subtracted from (g) to obtain the segmented wet scan (h).

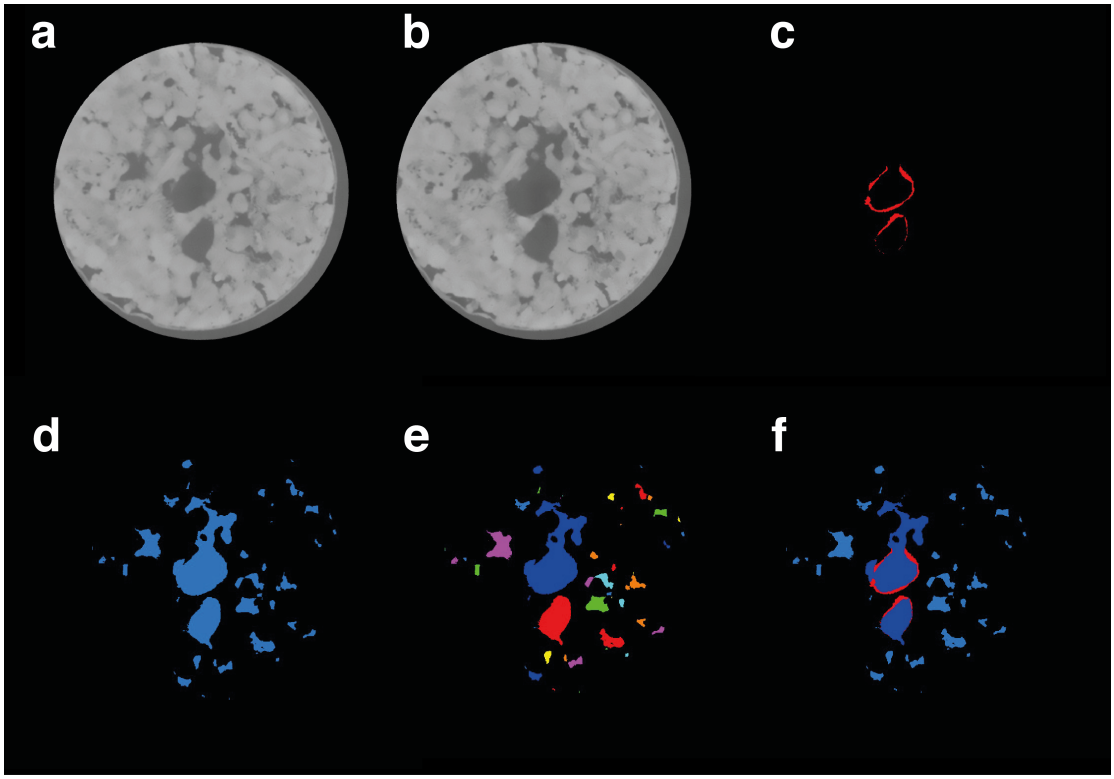

Figure 4 The channel analysis workflow. Raw scans pre (a) and post (b) reaction, the segmented difference (c), the entire segmented pore space (d), the segmented pore space labelled by channel (e), and the pore space separated into channels with reaction (dark blue) and channels without reaction (light blue) with the reacted voxels overlain red (f).

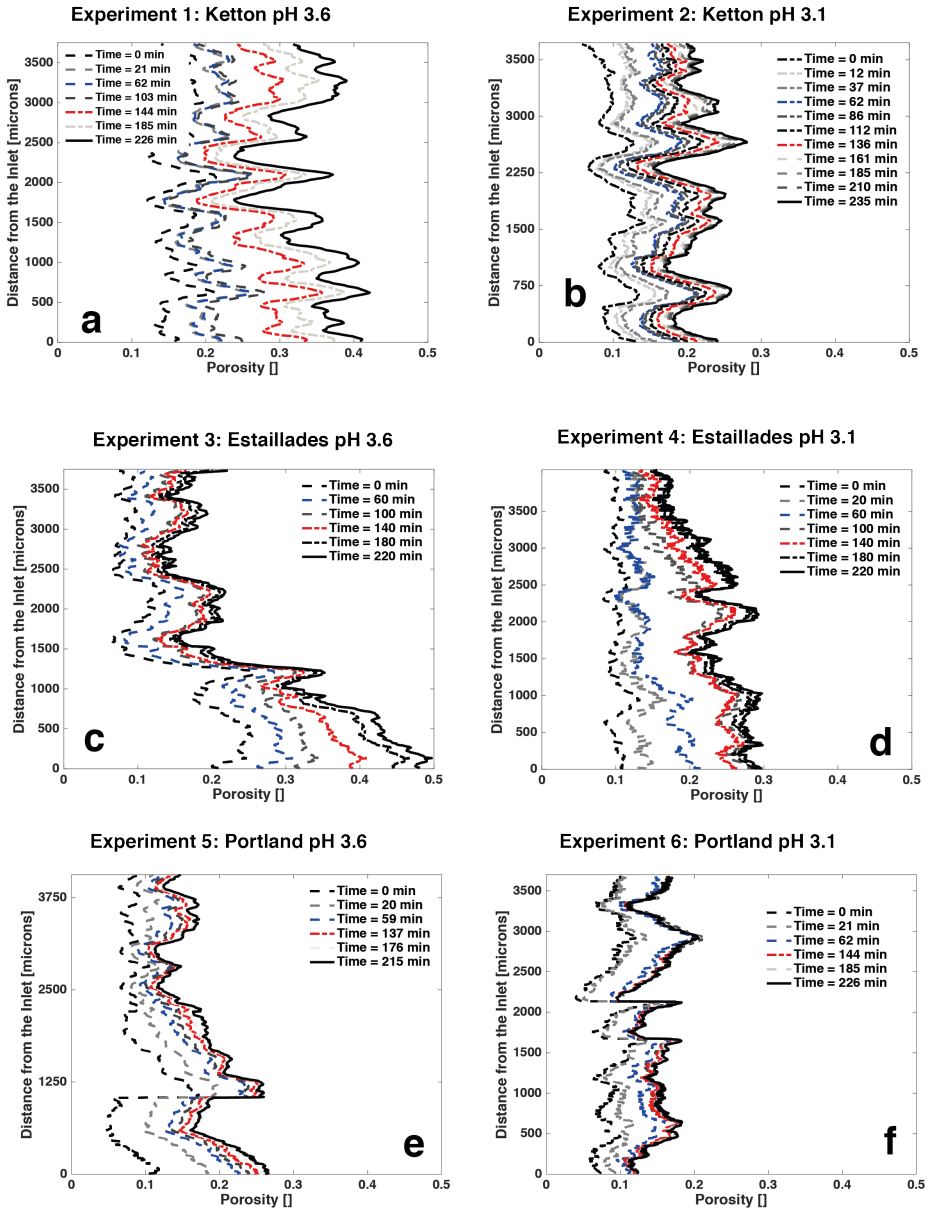

Figure 5 Sliced-averaged porosity versus distance from the sample inlet for Ketton at pH 3.6 (a) and pH 3.1 (b), Estaillades at pH 3.6 (c) and pH 3.1 (d) and Portland at pH 3.6 (e) and pH 3.1 (f). The blue and blue lines indicate ~1 and ~2 hours into the experiment. The inlet is defined as the beginning of the imaged portion of the sample closest to the inlet face of the core.

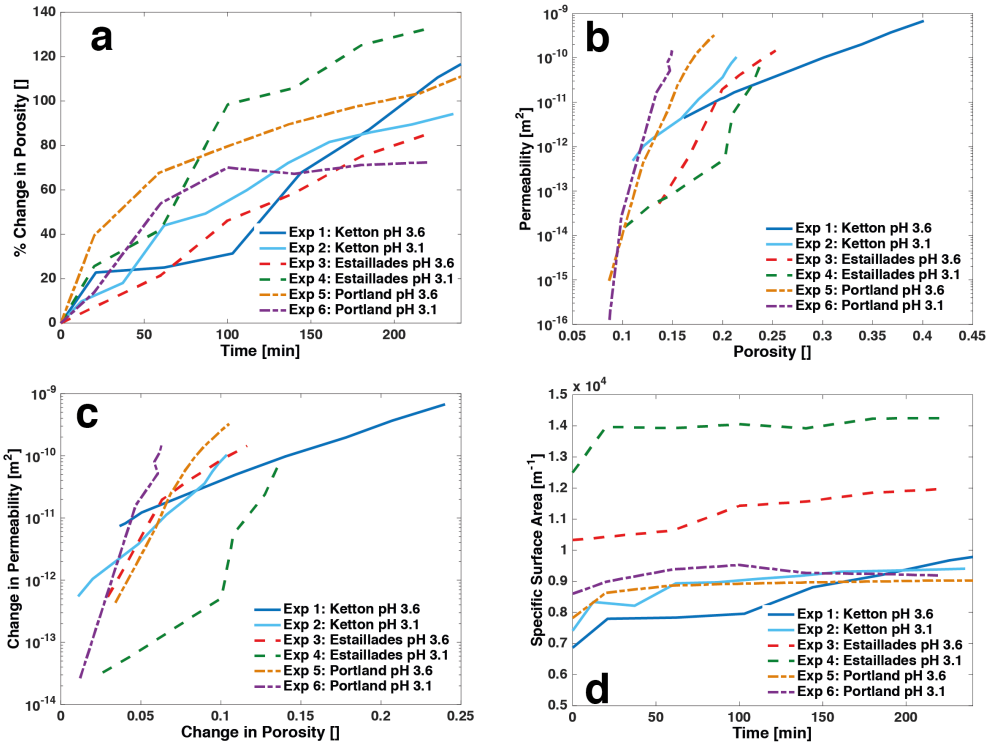

Figure 6 The percent change in average porosity across the whole sample versus time (a), permeability versus porosity (b), the change in permeability as a function of the change in porosity (c), and the specific surface area versus time (d) of Ketton, Estaillades, and Portland carbonates during dissolution. The porosity and surface area are calculated directly from the segmented images. Permeability is found from applying Darcy's Law from the computed flow field.

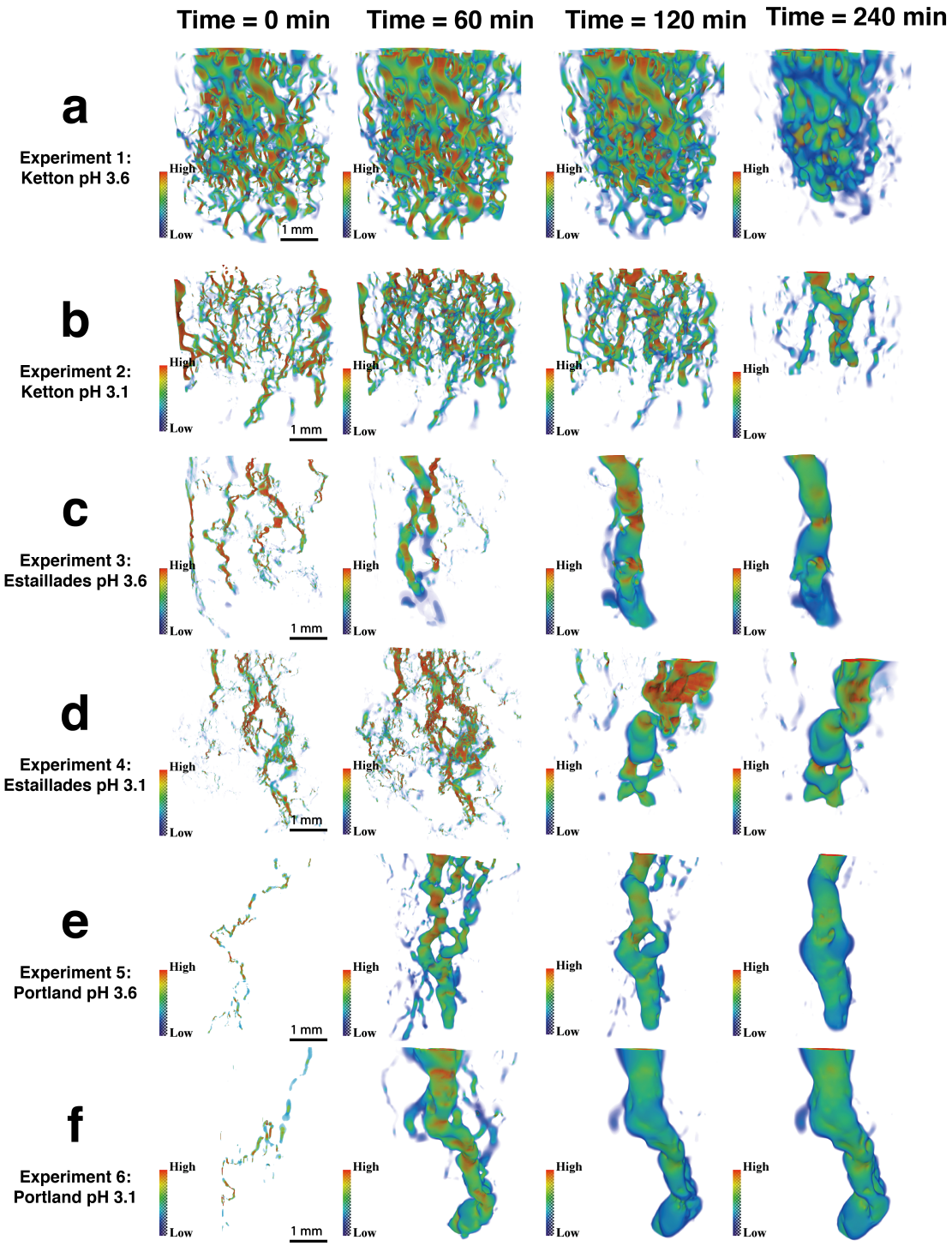

821

822 **Figure 7** The ratios of the magnitude of u at the voxel centres divided by the
823 average pore velocity U_{av} are coloured using a linear scale where low velocity is
824 blue, medium velocity is yellow, and high velocity is red.

825

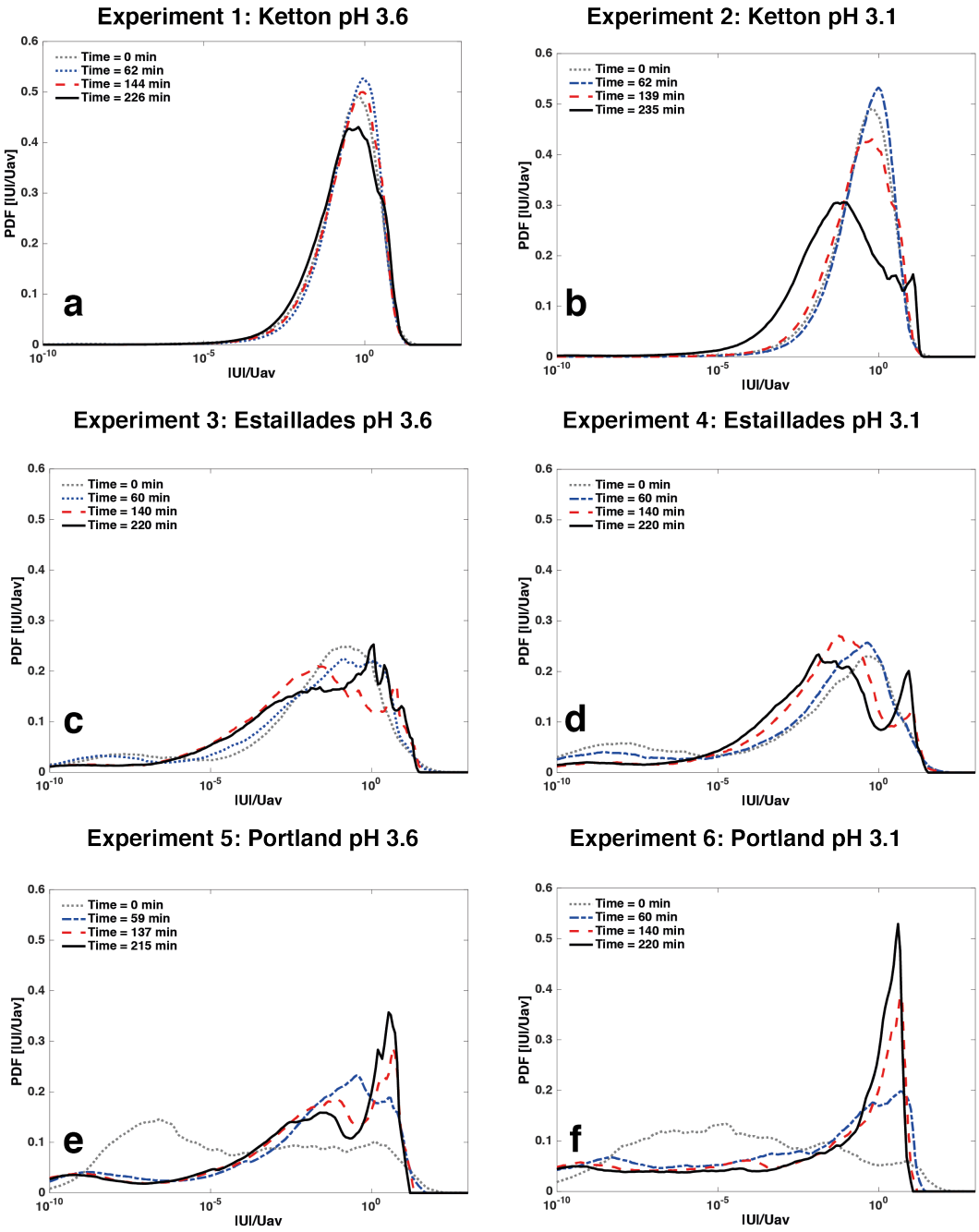

Figure 8 Probability density functions (PDFs) of pore voxel velocity during (a) experiment 1, (b) experiment 2, (c) experiment 3, (d) experiment 4, (e) experiment 5, (f) experiment 6. The velocity histogram is computed on the pore-space images and sampled uniformly in 256 bins of $\log(|\boldsymbol{u}|/U_{av})$, which are calculated as the ratios of the magnitude of u at the voxel centres divided by the average pore velocity U_{av}. The distributions are shown at times 0 (dotted line), ~60 (blue), ~120 (red), ~240 (solid black line) minutes.

835 **Table 3** Computed Flow and Reaction Parameters for times 0, ~60, ~120 and
836 ~240 min.

Time [min]	Property	Experiment 1: Ketton pH 3.6	Experiment 2: Ketton pH 3.1	Experiment 3: Estaillades pH 3.6	Experiment 4: Estaillades pH 3.1	Experiment 5: Portland pH 3.6	Experiment 6: Portland pH 3.1
0							
	absolute permeability (direct simulation) [m^2]	4.42×10^{-12}	4.81×10^{-13}	5.17×10^{-14}	1.53×10^{-14}	9.52×10^{-16}	1.25×10^{-16}
	image measured porosity ϕ_{CT} []	0.161	0.110	0.137	0.102	0.086	0.087
	image measured specific surface area S [m^{-1}]	6.86×10^{3}	7.41×10^{3}	1.03×10^{4}	1.25×10^{4}	7.82×10^{3}	8.60×10^{3}
	calculated L [m]	4.58×10^{-4}	4.24×10^{-4}	3.04×10^{-4}	2.51×10^{-4}	4.01×10^{-4}	3.65×10^{-4}
	calculated Pe [] [eq 3]	5.03×10^{2}	6.81×10^{2}	3.94×10^{2}	4.36×10^{2}	8.22×10^{2}	7.45×10^{2}
	calculated Da [] using batch reaction rate [eq 4]	4.70×10^{-5}	1.02×10^{-4}	$4..33 \times 10^{-5}$	1.02×10^{-4}	2.46×10^{-5}	7.80×10^{-5}
	calculated $PeDa$ []	2.36×10^{-2}	6.93×10^{-2}	1.71×10^{-2}	4.46×10^{-2}	2.02×10^{-2}	5.81×10^{-2}
	calculated reaction rate r_{eff} [$mol.m^{-2}s^{-1}$] [eq 6]	6.71×10^{-5}	4.57×10^{-5}	3.5×10^{-5}	1.85×10^{-5}	8.48×10^{-5}	2.71×10^{-5}
60							
	absolute permeability (direct simulation) [m^2]	1.26×10^{-11}	4.28×10^{-12}	5.88×10^{-13}	7.33×10^{-14}	6.31×10^{-12}	1.59×10^{-11}
	image measured porosity ϕ_{CT}	0.201	0.159	0.166	0.145	0.145	0.133

	[]						
	image measured specific surface area S [m^{-1}]	7.83×10^{3}	8.94×10^{3}	1.06×10^{4}	1.39×10^{4}	8.86×10^{3}	9.38×10^{3}
	calculated L [m]	4.01×10^{-4}	3.52×10^{-4}	2.95×10^{-4}	2.26×10^{-4}	3.54×10^{-4}	3.35×10^{-4}
	calculated Pe [] [eq 3]	3.52×10^{2}	3.92×10^{2}	3.15×10^{2}	2.75×10^{2}	4.33×10^{2}	4.44×10^{2}
	calculated Da [] using batch reaction rate [eq 4]	6.17×10^{-5}	1.55×10^{-4}	5.45×10^{-5}	1.53×10^{-4}	4.40×10^{-5}	1.27×10^{-4}
	calculated $PeDa$ []	2.18×10^{-2}	6.07×10^{-2}	1.72×10^{-2}	4.21×10^{-2}	1.93×10^{-2}	5.62×10^{-2}
	calculated reaction rate r_{eff} [$mol.m^{-2}s^{-1}$] [eq 6]	6.74×10^{-5}	1.71×10^{-5}	2.59×10^{-5}	1.07×10^{-5}	2.89×10^{-5}	1.44×10^{-5}
120							
	absolute permeability (direct simulation) [m^2]	5.39×10^{-11}	2.17×10^{-11}	4.03×10^{-11}	5.50×10^{-12}	5.66×10^{-11}	7.98×10^{-11}
	image measured porosity ϕ_{CT}[]	0.270	0.190	0.217	0.210	0.164	0.145
	image measured specific surface area S [m^{-1}]	8.81×10^{3}	9.17×10^{3}	1.16×10^{4}	1.39×10^{4}	8.96×10^{3}	9.27×10^{3}
	calculated L [m]	3.57×10^{-4}	3.42×10^{-4}	2.72×10^{-4}	2.62×10^{-4}	3.50×10^{-4}	3.39×10^{-4}
	calculated Pe [] [eq 3]	2.34×10^{2}	3.20×10^{2}	2.22×10^{2}	1.90×10^{2}	3.78×10^{2}	4.13×10^{2}
	calculated Da [] using batch reaction rate [eq 4]	9.06×10^{-5}	1.92×10^{-4}	7.57×10^{-5}	2.39×10^{-4}	5.09×10^{-5}	1.39×10^{-4}
	calculated	2.12×10^{-2}	6.14×10^{-2}	1.68×10^{-2}	4.55×10^{-2}	1.93×10^{-2}	5.76×10^{-2}

	PeDa []						
	calculated reaction rate r_{eff} [mol.m^{-2}s^{-1}] [eq 6]	3.27×10^{-5}	1.78×10^{-5}	7.01×10^{-6}	4.26×10^{-6}	5.77×10^{-6}	3.57×10^{-6}
240							
	absolute permeability (direct simulation) [m^2]	2.01×10^{-10}	1.04×10^{-10}	1.45×10^{-10}	6.44×10^{-11}	2.52×10^{-10}	1.47×10^{-10}
	image measured porosity ϕ_{CT} []	0.339	0.214	0.253	0.237	0.186	0.150
	image measured specific surface area S [m^{-1}]	9.67×10^{3}	9.41×10^{3}	1.20×10^{4}	1.43×10^{4}	9.19×10^{3}	1.43×10^{4}
	calculated L [m]	3.25×10^{-4}	3.34×10^{-4}	2.63×10^{-4}	2.20×10^{-4}	3.38×10^{-4}	3.42×10^{-4}
	calculated *Pe* [] [eq 3]	1.69×10^{2}	2.76×10^{2}	1.84×10^{2}	1.64×10^{2}	3.30×10^{2}	4.04×10^{2}
	calculated *Da* [] using batch reaction rate [eq 4]	1.26×10^{-4}	2.24×10^{-4}	9.28×10^{-5}	2.80×10^{-4}	5.95×10^{-5}	1.44×10^{-4}
	calculated *PeDa* []	2.13×10^{-2}	6.18×10^{-2}	1.70×10^{-2}	4.61×10^{-2}	1.96×10^{-2}	5.84×10^{-2}
	calculated reaction rate r_{eff} [mol.m^{-2}s^{-1}] [eq 6]	3.76×10^{-5}	8.71×10^{-6}	9.61×10^{-6}	4.26×10^{-6}	5.74×10^{-6}	1.16×10^{-6}

837

838

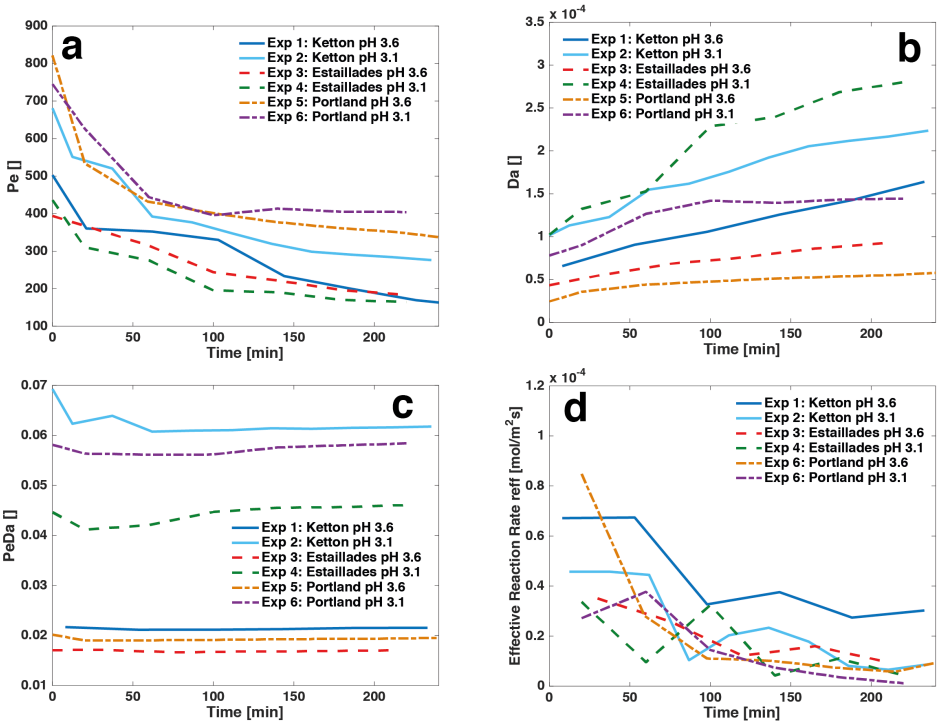

839

840 **Figure 9** (a) Péclet number (*Pe*), (b) Damköhler number (*Da*), (c) Péclet-
841 Damköhler number (*PeDa*), and (d) effective reaction rates (r_{eff}) for each
842 experiment through time.

843

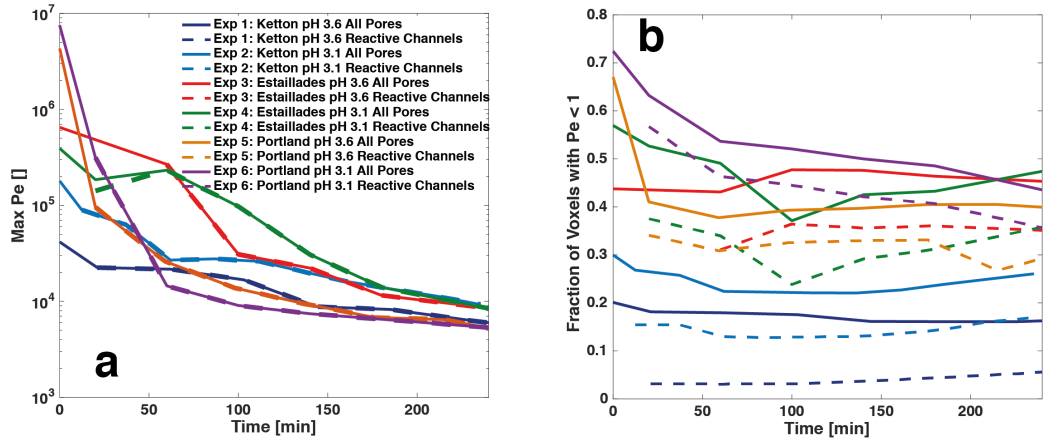

844

845 **Figure 10** (a) Maximum Péclet number (*Pe*) and (b) fraction of void voxels with
846 Péclet number (*Pe*) ≤ 1, measured by direct simulation for each experiment
847 through time both in the entire connected pore space (solid lines) and only in the
848 channel which have reacted during the previous tomographic scan period
849 (dashed lines).

850

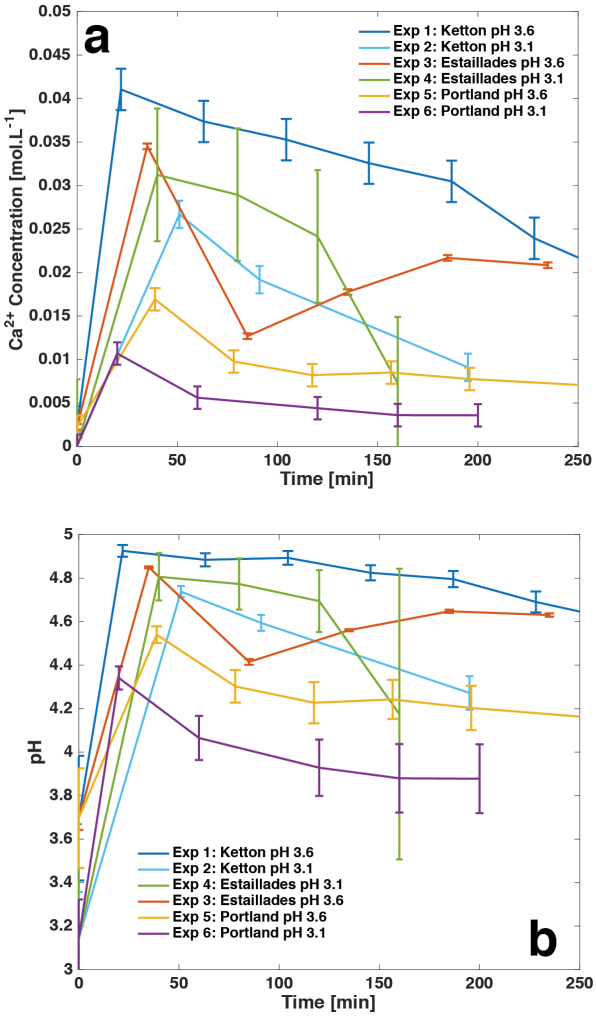

Figure 11 (a) Ca^{2+} concentration [$mol.L^{-1}$] measured in effluent and (b) pH as calculated from Ca^{2+} concentration by the method presented in Leal et al. (2014) versus time [min]. The error bars represent the standard error where $\sigma_x = \frac{\sigma}{\sqrt{n}}$, of the concentration and pH values. Each sample was taken over a period of 20 minutes. The points on the graph represent the beginning time of each 20-minute sampling period and the average values of concentration and pH during that period.

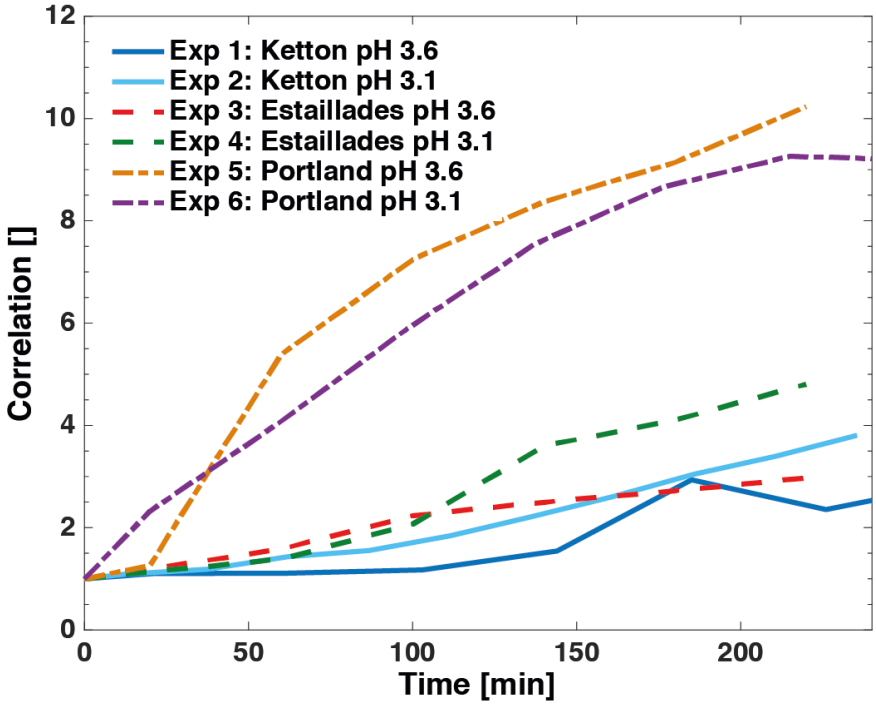

860

861 **Figure 12** Normalized correlation, Eqs. (1) and (2), between the initial voxel
862 velocities (time=0) and each those from successive image through time for each
863 experiment.

864

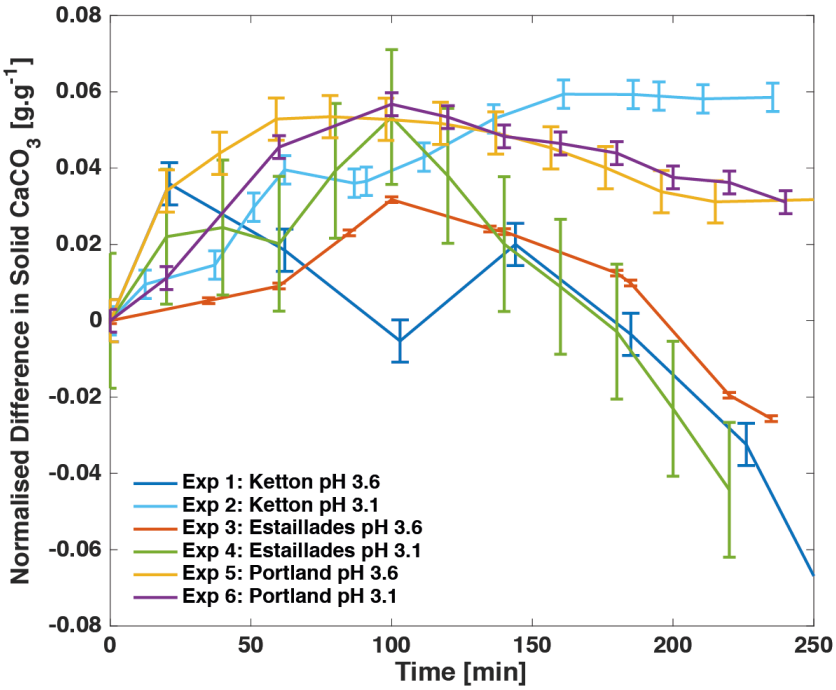

Figure 13 A comparison of effluent measured and CT observed fluid-solid reaction plotted as the difference in dissolved solid $CaCO_3$ versus time. The error bars represent the standard uncertainty of the effluent calcium content.

Table 4 The effective reaction rates calculated using the observed surface area of the pore space, the observed surface area of the reactive channels and the pH predicted from the effluent at time ~180 minutes. The error represents the standard error of the effluent calcium content.

Experiment #	Image observed All Pores r_{eff} [mol.m^{-2}s^{-1}] [eq 5]	Image observed Reactive Channels r_{eff} [mol.m^{-2}s^{-1}] [eq 5]	Effluent Calculated pH	Effluent Calculated r_{exp} [mol.m^{-2}s^{-1}] [eq 6]
Experiment 1: Ketton pH 3.6	3.27×10^{-5}	5.52×10^{-5}	4.80 ± 0.04	$1.6 \times 10^{-5} \pm 1.4 \times 10^{-6}$
Experiment 2: Ketton pH 3.1	8.09×10^{-6}	1.31×10^{-5}	4.27 ± 0.08	$5.5 \times 10^{-5} \pm 9.2 \times 10^{-6}$
Experiment 3: Estaillades pH 3.6	1.59×10^{-5}	3.10×10^{-5}	4.65 ± 0.01	$2.3 \times 10^{-5} \pm 5.3 \times 10^{-7}$
Experiment 4: Estaillades pH 3.1	1.10×10^{-5}	1.41×10^{-5}	4.17 ± 0.67	$6.8 \times 10^{-5} \pm 5.4 \times 10^{-5}$
Experiment 5:	3.57×10^{-6}	3.33×10^{-5}	4.20 ± 0.10	$6.4 \times 10^{-5} \pm 1.3 \times 10^{-5}$

Portland pH 3.6				
Experiment 6: Portland pH 3.1	7.46×10^{-6}	4.65×10^{-5}	3.88 ± 0.16	$1.4 \times 10^{-4} \pm 4.2 \times 10^{-5}$

875

876

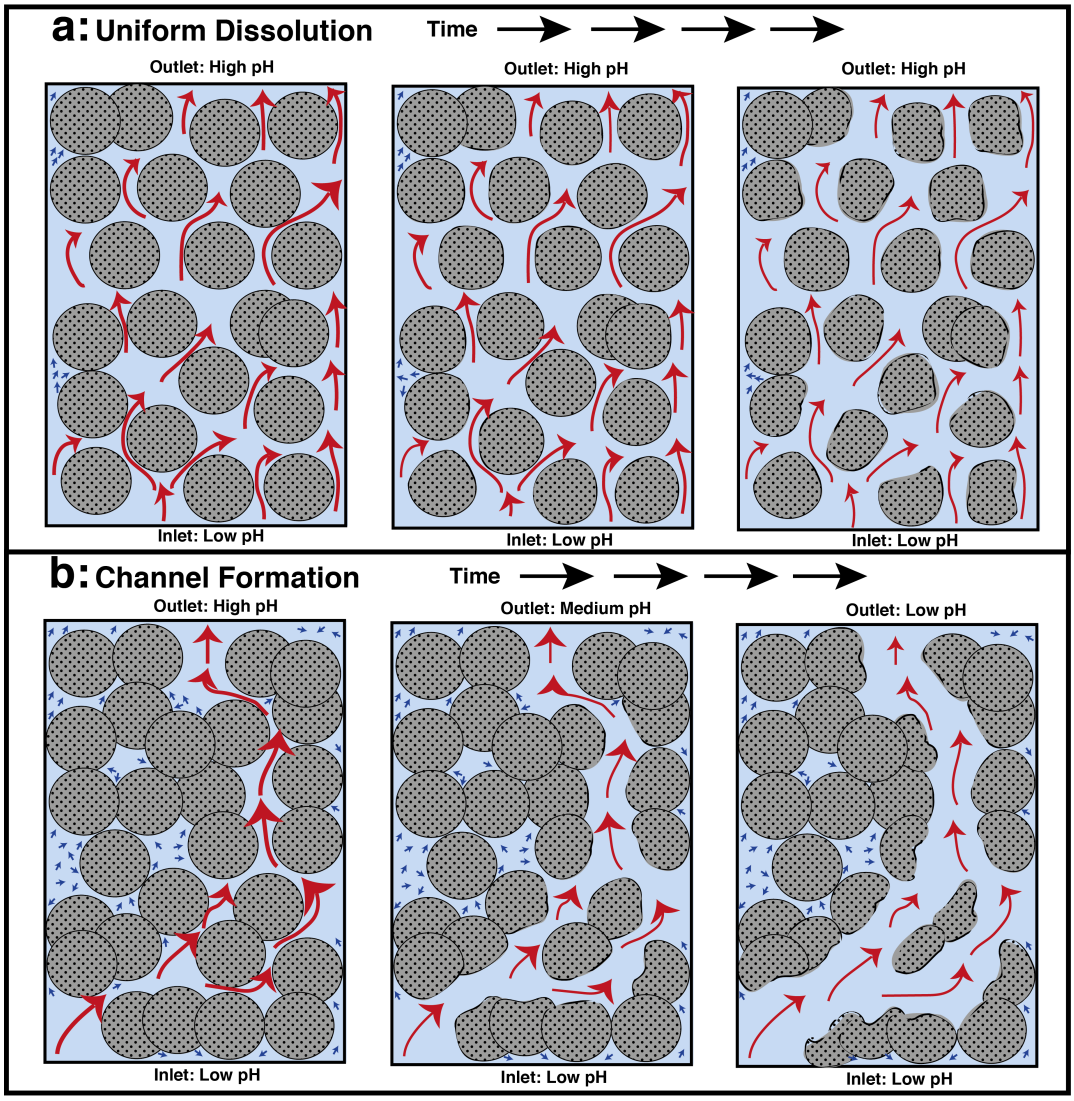

877

878 **Figure 14** A schematic of the flow and transport processes through time during
879 (a) uniform dissolution and (b) channel formation. Rock grains (grey circles) are
880 dissolved in advectively-dominated regions of fast flow (red arrows). Diffusive
881 regions (blue arrows) show little to no reaction.

882